Monthly Notices
of the
ROYAL ASTRONOMICAL SOCIETY

Mon. Not. R. Astron. Soc. **414,** 1827–1839 (2011) doi:10.1111/j.1365-2966.2011.18267.x

Multiphase dusty gas in the centre of NGC 4278

Yuping Tang,[1⋆] Qiusheng Gu,[2⋆] Shuinai Zhang[2] and Baitian Tang[2]

[1]*Department of Astronomy, Nanjing University, Nanjing 210093, China*
[2]*Key Laboratory of Modern Astronomy and Astrophysics (Nanjing University), Ministry of Education, Nanjing 210093, China*

Accepted 2010 December 24. Received 2010 December 20; in original form 2010 May 29

ABSTRACT

We present *Spitzer* spectroscopic mapping observations toward the central kpc region of the nearby elliptical low-ionization nuclear emission-line region (LINER) galaxy NGC 4278, using the Infrared Spectrograph (IRS). These observations reveal rich mid-infrared emission features of extended ionized gas, warm molecular hydrogen and dust. Different phases of gas and dust are closely related and belong to the same elongated feature. We further study the properties of multiphase dusty gas to uncover the underlying mechanism of ionization and excitation. The band ratio and intensity of PAH features in the central region might reflect the modified size distribution resulting from selective destruction. H_2 S(0)–S(7) pure rotational lines of molecular hydrogen show excessive intensity and moderately high excitation temperature compared with the photon dissociation region (PDR). A strong and extended [Si II] emission line is detected, which could be a sign of the reduced depletion of silicon in interstellar dust. We also discover an extended high-ionization region associated with enhanced H_2 S(1) emission. We conclude that a shock-heating component is required to account for the observed emission characteristics, which could be triggered by cloud–cloud interactions during the accretion of cold gas from the large H I disc.

Key words: galaxies: active – galaxies: elliptical and lenticular, cD – galaxies: individual: NGC 4278 – galaxies: nuclei – infrared: galaxies.

1 INTRODUCTION

A uniform, old stellar population and extremely hot gas ($T \sim 10^6$–10^7 K) were considered the only components of elliptical galaxies historically. However, recent studies confirm that cold and warm diffuse matter are not rare – although generally small in amount – in these systems. The Spectrographic Areal Unit for Research on Optical Nebulae (SAURON) Integral-Field Survey of Early-Type Galaxies (Sarzi et al. 2006) reported a 66 per cent detection of extended emission of gas for ellipticals, with a wide variety of spatial distributions and kinematic behaviour. Neutral hydrogen observations show that plenty of extended neutral hydrogen gas is clearly present in elliptical galaxies (Morganti et al. 2006; Noordermeer 2006). Moreover, an even cooler interstellar medium (ISM) including dust and molecular gas has been detected at a modest level (Knapp et al. 1989; Lauer et al. 2005; Wiklind, Combes & Henkel 1995; Sage, Welch & Young 2007).

The origin of both warm and cold matter in nearby elliptical galaxies still remains controversial; clarifying this issue is important for us to understand the ongoing physical processes that drive the evolution of this class of systems. In many cases, the warm and cold gas are linked with each other in nearby ellipticals (Morganti et al. 2006; Serra et al. 2008), suggesting the two components might be different phases of the same structure. For emission gas, line ratios typical of low-ionization nuclear emission-line regions (LINERs) are usually found in nearby ellipticals (Ho, Filippenko & Sargent 1997; Filippenko 2003). A variety of mechanisms have been applied to interpret its energy source. Besides photoionization by the active nucleus and low-level residual star formation, the possibilities of photoionization by an old, hot stellar population (Binette et al. 1994; Macchetto et al. 1996), cooling flow or thermal interaction with hot gas (Sparks, Macchetto & Golombek 1989; de Jong et al. 1990; Fabian 1994) and heating via shocks (Dopita & Sutherland 1995) were also discussed and examined by previous authors, while a conclusive answer has not yet been reached. On the other hand, the lack of any significant correlation between the cold diffuse matter and stars in both mass and kinematics in nearby ellipticals might be a sign of an external origin for the former content (Knapp, Turner & Cunniffe 1985; Goudfrooij et al. 1994; Oosterloo et al. 2002), although the continuous thermal and dynamical evolution of ellipticals, such as heating of stellar ejecta through random collision, might assist in obscuring such a relationship.

The nearby ($D = 16.1$ Mpc; Tonry et al. 2001), isolated elliptical galaxy NGC 4278 is part of a rare sample of ellipticals with detections of multiphase ISM, thus offering a significant opportunity to study the evolution of gaseous matter in such an environment. Among the first ellipticals for which cold gas was detected,

⋆E-mail: tangyping@gmail.com (YT); qsgu@nju.edu.cn (QG)

NGC 4278 has long been known for its massive ($\sim 10^8\,M_\odot$) regular H I disc extending beyond 5 kpc. Further more, the detection of CO emission was recently reported by Combes, Young & Bureau (2007). Strong emission produced by ionized gas was revealed by the SAURON survey (Sarzi et al. 2006), which kinematically coincides well with the H I disc (Morganti et al. 2006) and shows asymmetrical substructures with high ionization. In optical images, NGC 4278 shows large-scale dust patches located north and north-west of the galaxy centre (Lauer et al. 2005), which might contribute to the excess far-infrared emission detected by the *IRAS* (Knapp et al. 1989) and *ISO* (Temi et al. 2004) infrared space telescopes. Additionally, mid-infrared extended, non-stellar emission possibly related to the reprocessing of UV/optical radiation by polycyclic aromatic hydrocarbons (PAHs) is shown in the *Spitzer* InfraRed Array Camera (IRAC) image after removing the stellar contribution (Tang et al. 2009).

In this work, we present mid-infrared spectral mapping observations of the *Spitzer* space telescope toward the central kpc region of NGC 4278. There are several reasons why spatially resolved mid-infrared spectroscopy in such an area is interesting. First, it allows us to carry out analysis on spectra without suffering from serious dust extinction; secondly, the uniform spectral and spatial stellar background of this elliptical galaxy provide us with the chance to identify activities characterized by low surface brightness; thirdly, mid-infrared spectra contain emission features from the multiphase ISM, including dust, warm molecular hydrogen and ionized gas, thus enabling us to explore the underlying heating mechanism in various aspects. Our ultimate goal is to understand the origin and evolution of cold and warm matter in this LINER galaxy.

This paper is organized as follows. The observation and data reduction are described in Section 2. The emission-line maps are shown in Section 3. We explore the physical properties of cold and warm matter from observations in Section 4 and carry out a discussion on the possible energy source behind the diffuse matter in Section 5. In Section 6 we draw our conclusions.

2 OBSERVATIONS AND DATA REDUCTION

We download the IRS Basic Calibrated Data (BCD) of NGC 4278 from the archive of the *Spitzer* Science Center (Programme ID: 30471, PI: J. D. Smith). This programme is aimed at investigating the nature of PAH emission features in nearby galaxies hosting low-luminosity active galactic nuclei (AGNs). The observations were obtained in low-resolution spectral mapping mode with a spectral resolution $R \sim 60$–130, using the short–low (SL: 5–15 μm) and long–low (LL: 14–38 μm) modules and taken on 2007 February 9.

The SL spectral mapping covers 1×10 map positions with a step size of 1.85 arcsec in the perpendicular direction. Observations consist of 60-s ramp duration with 3 circles per step. The observations obtained by the LL module consist of 4×11 map positions with a step size of 5.08 arcsec in the perpendicular direction and 15.0 arcsec in the parallel direction, 30-s ramp duration was used with 1 circle per step. The mapping area is shown in Fig. 1.

Primary data reduction was carried out with the *Spitzer* Science Center (SSC) pipeline, version S18.7.0, for both SL and LL modules, including standard reductions such as removal of electron bias, dark-current subtraction and flat-field correction. We further use the IDL-based software package CUBISM (Smith et al. 2007a) to extract and combine spectra into a single spectral cube. Background subtraction was performed using off-source observations accompanying each map, which were taken in a region containing no spectral signatures using the same slit pattern and exposure time

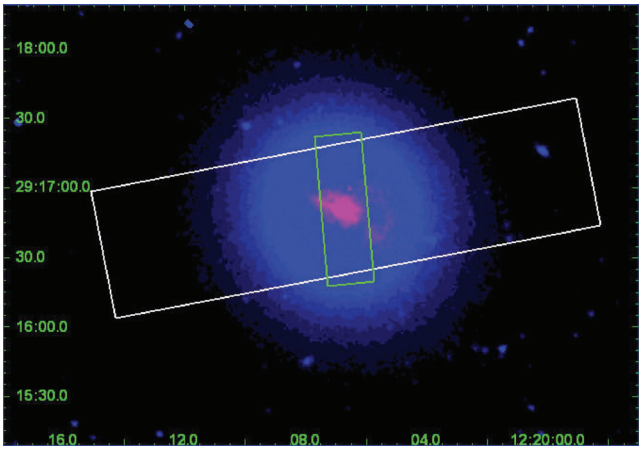

Figure 1. Mapping area of NGC 4278. Blue: IRAC 3.6 image. Red: IRAC 8.0 non-stellar emission, derived by subtracting a scaled IRAC 3.6 image from the IRAC 8.0 image (Tang et al. 2009). White box: mapping coverage of long-slit observations. Green box: mapping coverage of short-slit observations. See the electronic version of the article for a colour version of this figure.

with the mapping sequence. After background subtraction, the major artefacts remaining in the two-dimensional map of the data cube are some bright 'stripes', which are caused by bad pixels rastered across the map. The bad pixels are removed by carefully examining each wavelength of the panel with the backtracking tool in CUBISM.

3 EMISSION-LINE DISTRIBUTION

Ionized gas in NGC 4278 has previously been studied by Sarzi et al. (2006, 2010) based on the observations of the SAURON survey. Fig. 2 shows the distribution of [O III]λ5007 emission obtained by SAURON observations (kindly provided by Marc Sarzi) overplotted with the contours of IRAC 8-μm excess non-stellar emission; the latter is obtained by subtracting a scaled IRAC 3.6-μm image from the IRAC 8-μm image. In Tang et al. (2009), we showed that for quiescent ellipticals [3.6]–[8.0] colours are generally constant and

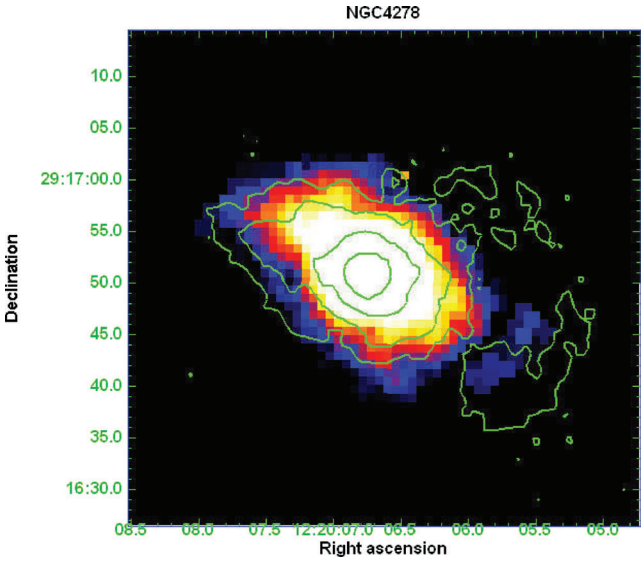

Figure 2. [O III]λ5007 emission-line map, overlaid with contours of IRAC 8.0 non-stellar emission. Contour levels are given as: 1.50, 0.61, 0.25, 0.10 (in units of MJy sr^{-1}).

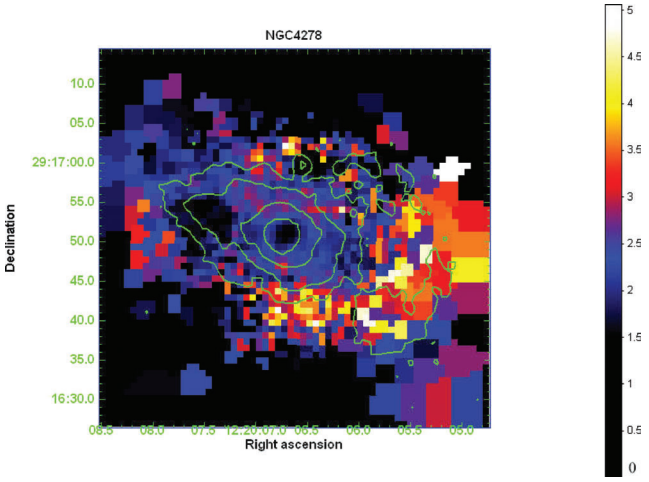

Figure 3. Line-ratio map of [O III]λ5007/Hβ, overlaid with contours of IRAC 8.0 non-stellar emission. Contour levels are as in Fig. 2.: 1.50, 0.61, 0.25, 0.10 (in units of MJy sr^{-1}).

change little with radius from the centre. We can simply multiply the 3.6-μm image by a constant to account for the contribution of an old stellar population at 8.0 μm, then degrade this image to 8.0 μm and subtract it from the original 8-μm image. For NGC 4278 this constant, which reveals the infrared colour of old stars, is taken as 0.29. The central elongated feature along the south-west–north-east direction with a position angle of 70° generally coincides with the [O III]λ5007 distribution. Further, both [O III]λ5007 and Hβ emission are spatially and kinematically consistent with the inner part of the H I disc in NGC 4278 (Morganti et al. 2006), suggesting that dust, cold gas and warm gas simply belong to different phases of the same gaseous rotational structure.

Another important result of SAURON observations for NGC 4278 is a 'reverse' distribution of ionization states for warm gas in the central region. The nucleus shows a lower degree of ionization compared with the outer circumnuclear region. In Fig. 3 we present a map of the [O III]λ5007/Hβ ratio along with the IRAC 8-μm non-stellar emission. A low-surface-brightness, high-ionization ring-like structure extends beyond 10 arcsec and is obvious in the southern and western areas. This feature, together with the fact that the radial profile of Hβ flux is more extended than expected for photoionization by the central AGN (Sarzi et al. 2010), strongly suggests a second ionization source that dominates over the area outside the central 5 arcsec. The IRAC 8-μm non-stellar emission also shows extended patchy structures to the west of the main feature. As already noticed by Sarzi et al., the western patchy structures seem to be anticorrelated with the distribution of ionization degree, with some subareas of low PAH 7.7-μm covering having the highest [O III]λ5007/Hβ ratio. The authors suggested that this feature could be explained by the local hardening of the ionizing continuum and the decline of the ionization parameter due to dust effects. It is interesting to notice that there is no such area with irregular [O III]λ5007/Hβ distribution on the north-east side of the main elongated structure, where the surface brightness of 8 μm excess is higher than in the patchy regions.

We construct line maps from *Spitzer* mapping observations by applying a standard spectral decomposition method (PAHFIT) for each pixel. Details of PAHFIT will be discussed in Section 4. We also compare each emission-line map with IRAC 8-μm non-stellar emission. To do this, we first degrade the resolution of the IRAC 8.0 image to that of each line map by Gaussian convolution. The scale of the

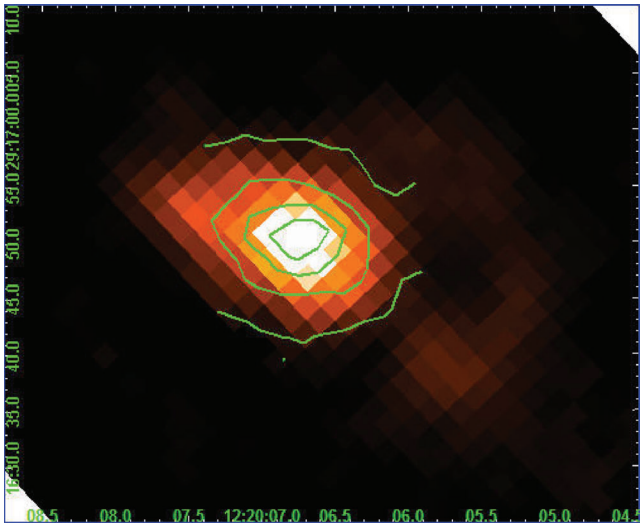

Figure 4. IRAC 8.0 non-stellar emission image, overlaid with contours of PAH 11.3. Contour levels are given as 12.1, 8.54, 4.93, 1.33 (in units of 10^{-22} erg s^{-1}), where the lowest contour level corresponds to 3σ significance.

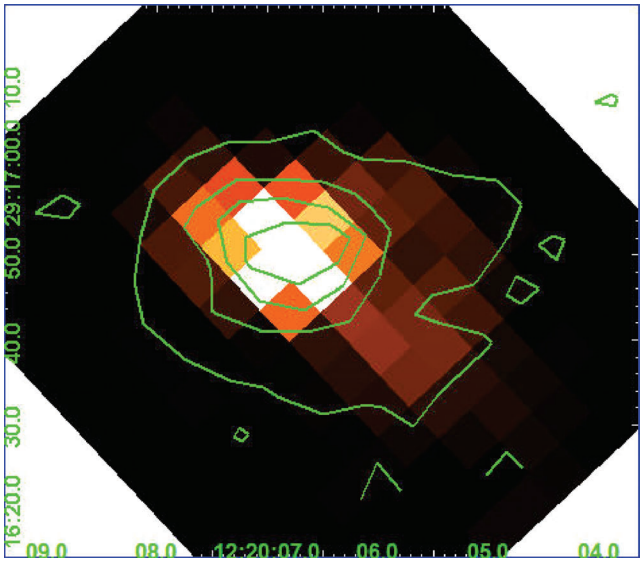

Figure 5. IRAC 8.0 non-stellar emission image, overlaid with contours of PAH 17. Contour levels are given as 2.41, 1.67, 0.94, 0.20 (in units of 10^{-21} erg s^{-1}), where the lowest contour level corresponds to 3σ significance.

Gaussian kernel is determined by matching the point-spread function (PSF) of the IRAC 8.0 image with the PSF at the wavelength of the line centre. After convolution, the IRAC 8-μm image is rebinned to the same pixel size as each line map.

In Figs 4 and 5 we show distributions of PAH 11.3-μm and PAH 17-μm band emission respectively, overlaid on IRAC 8-μm non-stellar emission. For PAH 11.3 μm, the mapping area has not covered the entire PAH emission region. Nevertheless, the two distributions agree well with each other for the central elongated feature, supporting the validity of using the latter distribution to trace PAH 7.7-μm emission. The spatial distribution of PAH 17 μm, however, does not totally coincide with that of the IRAC 8-μm excess. PAH 17 μm is distributed in a more symmetrical pattern relative to IRAC 8-μm excess.

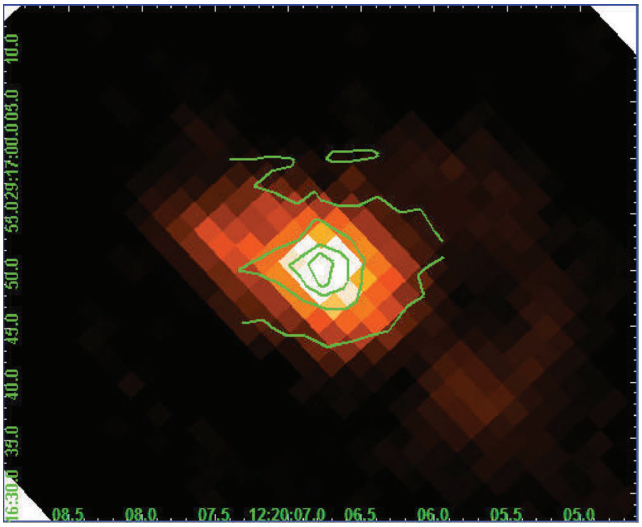

Figure 6. IRAC 8.0 non-stellar emission image, overlaid with contours of H_2 S(3). Contour levels are given as 4.73, 4.00, 3.31, 2.33, 1.81, 1.36, 0.38 (in units of 10^{-22} erg s^{-1}), where the lowest contour level corresponds to 3σ significance.

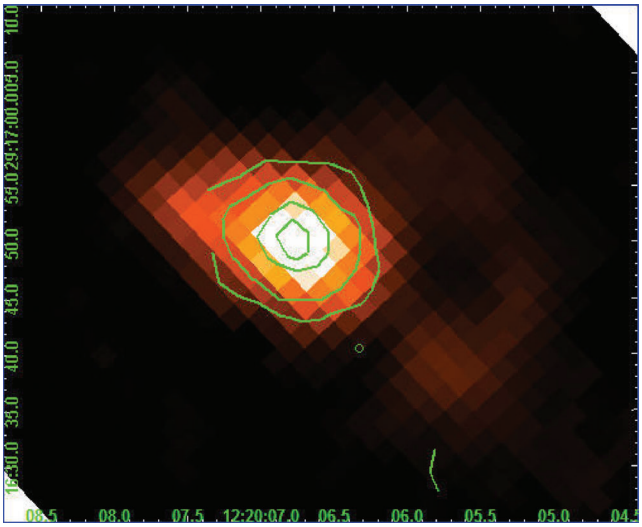

Figure 8. IRAC 8.0 non-stellar emission image, overlaid with contours of [Ne II] 12.8 μm. Contour levels are given as 3.45, 1.70, 0.64, 0.29 (in units of 10^{-22} erg s^{-1}), where the lowest contour level corresponds to 3σ significance.

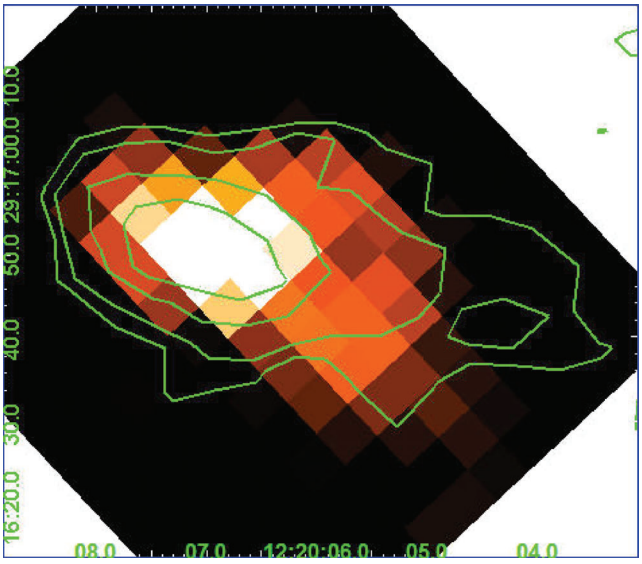

Figure 7. IRAC 8.0 non-stellar emission image, overlaid with contours of H_2 S(1). Contour levels are given as 4.10, 2.22, 1.09, 0.72 (in units of 10^{-22} erg s^{-1}), where the lowest contour level corresponds to 3σ significance.

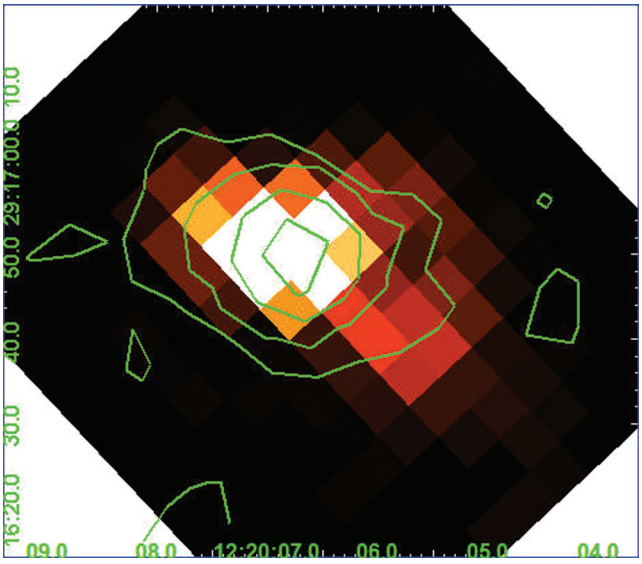

Figure 9. IRAC 8.0 non-stellar emission image, overlaid with contours of [Ne III] 15.6 μm. Contour levels are given as 6.34, 3.20, 1.31, 0.68 (in units of 10^{-22} erg s^{-1}), where the lowest contour level corresponds to 3σ significance.

In Figs 6 and 7 we present the distribution of H_2 S(3) (mapped in the SL module) and H_2 S(1) (mapped in the LL module) pure rotational lines of molecular hydrogen. For S(3), the distortion of contours on the northern edge of the main feature results from removal of a series of severe global bad pixels and does not necessarily imply a true turbulence. Still, it is obvious that both S(3) and S(1) emission generally follows PAH emission. The H_2 S(1) distribution is slightly more extended than the PAH patchy structures west of the main feature. We notice that the flux peak of the H_2 S(1) map deviates from that of the IRAC 8-μm image by about 4 arcsec, which is slightly smaller than the pixel size (5.08 arcsec) of LL orders and needs to be further confirmed.

Figs 8–10 show the distribution of fine-structure lines for [Ne II] 12.8 μm, [Ne III] 15.6 μm and [Si II] 34.8 μm. With their ionization potential spreading over a wide range, ionized emission lines show considerable difference from PAH features and H_2 pure rotational lines. In particular, for high-ionization line [Ne III] (with an ionization potential of 41.0 eV), the central distributions are more symmetrical within the central 10 arcsec compared with PAHs and warm molecular hydrogen emissions, although still showing a faint elongated feature consistent with the position angle of the latter two distributions. For the strong [Si II] emission (with a lower ionization potential of 8.2 eV), its sufficiently high signal-to-noise (S/N) ratio reveals a more extended component, which departs from the extended patchy distribution of PAHs and H_2 S(1) emission.

In Fig. 11, we present *Chandra* X-ray observations of the diffuse soft X-ray emission with the point source removed (it will be present in Zhang et al., in preparation), overlaid with the

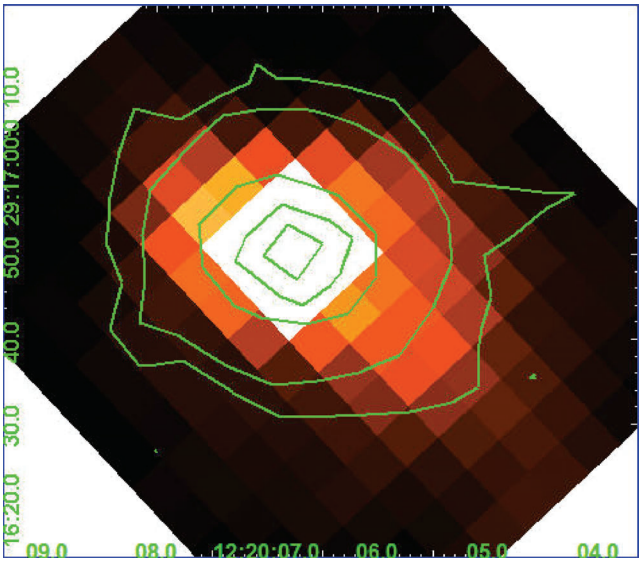

Figure 10. IRAC 8.0 non-stellar emission image, overlaid with contours of [Si II] 34.8 μm. Contour levels are given as 16.60, 9.71, 4.80, 1.85, 0.87 (in units of 10^{-22} erg s^{-1}), where the lowest contour level corresponds to 3σ significance.

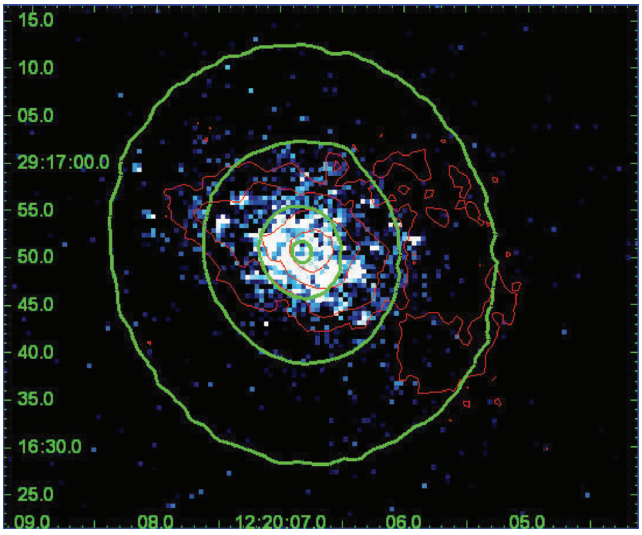

Figure 11. *Chandra* 0.2–1.5 keV diffuse emission image removed from point sources, overlaid with contours of the IRAC 3.6 image (green) as well as contours of IRAC 8.0 non-stellar emission (red). Contours levels of the IRAC 3.6 image are given as 23.22, 6.46, 1.80, 0.50 (in units of MJy sr^{-1}). Contour levels of IRAC 8.0 non-stellar emission are as in Fig. 2.: 1.50, 0.61, 0.25, 0.10 (in units of MJy sr^{-1}). See the electronic version of the article for a colour version of this figure.

contours of the IRAC 3.6 emission as well as the IRAC 8 non-stellar emission. While lacking an extended X-ray halo, the bulk of the diffuse emission is confined to the central region and is generally consistent with the distribution of IRAC 8.0 non-stellar emission. The elongated feature of the X-ray diffuse emission has previously been noticed by Terashima & Wilson (2003); this coincidence with warm gas might suggest a connection between the two phases of gaseous matter in the centre. We also notice that recently Younes et al. (2010) found a temperature of 0.4 ± 0.1 keV for the thermal component in the central 10-arcsec region.

4 SPECTRA OF NUCLEAR AND EXTENDED REGIONS

Spectra of the nuclear region are extracted from an 8-arcsec circular aperture centred at the surface-brightness peak of the continuum. The mid-infrared emission in NGC 4278 is extended; we need to use a slit loss-correction function (SLCF hereafter) to correct the original flux calibration provided by the SSC based on a point source, which overestimates the flux by neglecting the flux accepted from outside the slit. Currently the SLCF is built on a simple assumption that the extended emission is uniform and unlimitedly extended (Smith et al. 2007a). Unfortunately, this assumption is not well satisfied in the case of NGC 4278, which shows a considerable degree of surface-brightness concentration. The application of the SLCF leads to two artefacts in the spectra. First, a significant mismatch appears at the boundary of SL2 and LL1, where the flux density of SL1 is 20 per cent higher than that of LL2. This mismatch happens because the slit width and pixel size in the LL module are nearly three times those in SL. At the same wavelength, the SLCF would overcorrect LL spectra in comparison with SL, because the real 'excess' flux coming from outside the slit is relatively less in LL due to concentration of the extended emission. Another artefact is more complex. Since the SLCF depends on PSF sizes at different wavelengths, application of this correction would modify the spectral profile. We estimate these two effects by the following steps. First, we directly match LL to SL by multiplication: this spectrum will be referred to as the 'matched spectrum' hereafter. Secondly, we disable the SLCF for LL spectra – this would elevate LL spectra by about 17 per cent at the blue end, thus filling the gap between SL and LL – then perform a minor adjustment to scale LL to SL by multiplication. The resulted spectrum is called the 'uncorrected spectrum' hereafter. The two spectra are shown in Fig. 12. The disagreement between the two spectra is lower than 10 per cent blueward of 20 μm but becomes significant at longer wavelengths. In this work, three lines of interest, H_2 S(0), [S III] 33.5 μm and [Si II] 34.8 μm, fall at wavelengths longer than 20 μm; discussions depending on the relative strengths of these lines will be treated with caution.

We further compared the spectra with IRAC and Multiband Imaging Photometer (MIPS) photometry results derived from

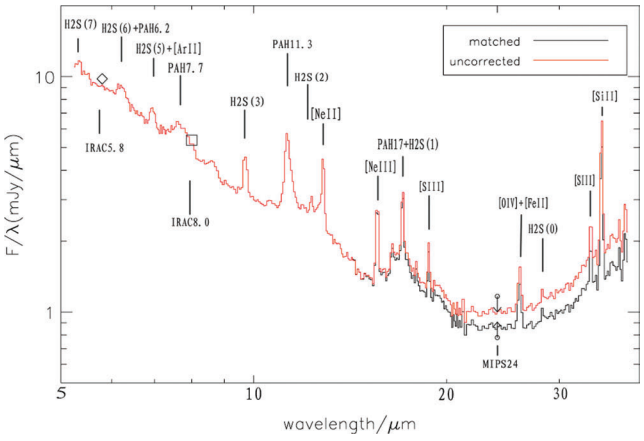

Figure 12. Spectra extracted from the central 8-arcsec aperture, overplotted with IRAC 5.8 (diamond), IRAC 8.0 (square) and MIPS 24 (circle plus arrow) photometry data points. The black sold line is the matched spectrum with LL orders corrected by SLCF, the red solid line is the uncorrected spectrum with LL orders uncorrected by SLCF. See the electronic version of the article for a colour version of this figure.

the same aperture. For the data reduction of IRAC data we started from the BCD images and followed the same steps as in Tang et al. (2009), while for MIPS data we started from the post-BCD image. We employed the extended source-aperture correction for calibration developed by Tom Jarrett.[1] For MIPS images, unfortunately, such a correction is not available. Thus we only give an estimation of lower and upper limits from the data. The lower limit is derived by directly integrating the counts within the aperture without an aperture correction, while the upper limit is derived by employing an aperture correction for a point source, as provided in the MIPS Instrument Hand Book;[2] since such an aperture correction ignores the diffraction of light from outside the aperture, it would overestimate the real flux. The results are shown in Fig. 12. The IRAC photometry points are consistent with our spectra within the calibration uncertainty (∼10 per cent, Fazio et al. 2004), indicating that the flux calibration based on SLCF is reliable for SL observations. The MIPS photometry data fail to help to distinguish between the matched spectrum and uncorrected spectrum.

Hereafter, we will carry out discussions based on results from the uncorrected spectrum, since the mismatch between the SL and LL modules indicates that the SLCF correction based on the assumption of a uniform extended source is not proper for LL observations. We caution the readers that this approach is not a precise solution. Nevertheless, this will not bring significant influence on the spectral shape shortward of 20 μm, although it might overestimate the line flux by no more than 30 per cent at the longest wavelength. (For [Si II] 34.8 μm, the line flux derived from the uncorrected spectrum is 29.3 per cent higher than that from the matched spectrum.)

We use the package PAHFIT (Smith et al. 2007b) to fit the full 5–38 μm spectrum. PAHFIT applies three sets of components (thermal continuum produced by stars and dust; PAH features; emission lines of ion species and molecular hydrogen) to separate different emission components. Throughout this article, the error bars are directly given by CUBISM and PAHFIT. In CUBISM, only BCD-level statistical uncertainty estimates produced by the IRS pipeline from deviations of the fitted ramp slope are considered when building error cubes; other uncertainties are not taken into consideration (Smith et al. 2007a). The errors for combined quantities, such as integrated intensities, estimated are formulated using the full covariance matrix by CUBISM (Smith et al. 2007b), which is based on the Levenberg–Marquardt algorithm. It should be noted that systematic calibration uncertainty is not accounted for here. We estimate it to be not larger than 10 per cent by comparing SL spectra with IRAC 5.8-μm and 8.0-μm monochromatic flux density (Fig. 12). However, in this research most discussions are based on the relative strengths of spectral features, where calibration uncertainty cancels out. The result of spectral decomposition is shown in Fig. 13. Generally, the observation could be successfully reproduced by a combination of various components. The spectrum shows no sign of silicate absorption around 10 μm, coinciding with the result derived from the Balmer decrement (Ho et al. 1997). The only significant spectral feature unable to be constructed by models is the 18–20 μm plateau possibly caused by large PAH molecules, simply because PAHFIT excludes this feature from consideration. Smith et al. (2007b) suggested this plateau-like extension is not correlated with the PAH 17-μm feature. Another potential problem underlying the PAHFIT procedure is that it only considers silicate absorption. As pointed out by Bregman, Temi & Bregman (2006) and Kaneda et al. (2008), for early-type galaxies the silicate emission feature around 10 μm originating from the circumstellar envelope of asymptotic giant branch (AGB) stars might affect the measurement of the PAH feature at 7.7 μm. This effect will be estimated in the next section. The results of decomposition for the central 8-arcsec aperture are shown in Table 1.

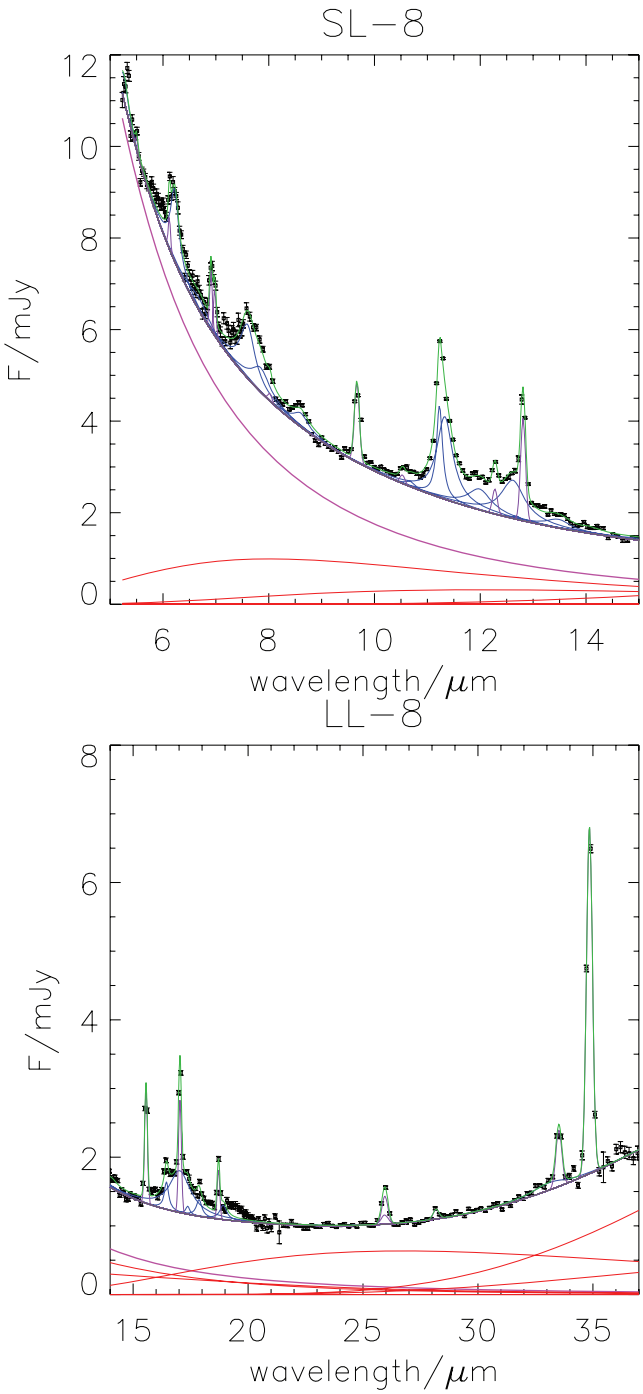

Figure 13. Full decomposition of uncorrected spectra extracted from the central 8-arcsec aperture. The magenta line shows the stellar continuum, red solid lines represent the multitemperature thermal dust components and the grey line is the summation of the stellar and dust continua. Blue lines show PAH emission features, violet lines represent emission arising from warm molecular hydrogen and ionized species. Upper: 5–15 μm, Lower: 15–37 μm. See the electronic version of the article for a colour version of this figure.

[1] http://spider.ipac.caltech.edu/staff/jarrett/irac/calibration/
[2] http://ssc.spitzer.caltech.edu/mips/mipsinstrumenthandbook/

Table 1. Emission-line strengths in the central 8-arcsec aperture.

Line	Flux (m)[a] (10^{-21} W cm $^{-2}$)	Flux (uc)[b] (10^{-21} W cm $^{-2}$)
PAH 6.2 μm	22.60 ± 0.74	22.50 ± 0.74
PAH 7.7 μm	41.30 ± 2.46	40.80 ± 2.47
PAH 11.3 μm	38.60 ± 0.24	38.60 ± 0.24
PAH 12.6 μm	17.20 ± 0.48	17.00 ± 0.49
PAH 17 μm	22.00 ± 0.39	23.80 ± 0.48
H_2 S(0)	0.40 ± 0.04	0.48 ± 0.06
H_2 S(1)	4.27 ± 0.10	4.48 ± 0.13
H_2 S(2)	1.56 ± 0.07	1.56 ± 0.07
H_2 S(3)	6.26 ± 0.09	6.26 ± 0.09
H_2 S(5)	3.53 ± 0.27	3.53 ± 0.27
H_2 S(6)	1.80 ± 0.22	1.80 ± 0.22
H_2 S(7)	0.83 ± 0.24	0.84 ± 0.24
[Ar II] 7.0 μm	2.78 ± 0.26	2.78 ± 0.26
[S IV] 10.5 μm	0.62 ± 0.09	0.62 ± 0.09
[Ne II] 12.8 μm	6.14 ± 0.09	6.13 ± 0.09
[Ne III] 15.6 μm	4.82 ± 0.11	4.95 ± 0.14
[S III] 18.7 μm	1.50 ± 0.07	1.65 ± 0.09
[S III] 33.5 μm	1.88 ± 0.07	2.39 ± 0.10
[Si II] 34.8 μm	11.00 ± 0.09	14.10 ± 0.15

[a] Spectra with LL orders corrected by SLCF and matched to SL orders.
[b] Spectra with LL orders uncorrected by SLCF.

The nuclear spectra of NGC 4278 are somehow beyond the ordinary elliptical galaxies as regards abundance of emission features. In contrast, the continuum generally follows blackbody radiation from an old stellar population, with some marginal contribution from hot and warm dust. The emission features appearing in the mid-infrared spectra of NGC 4278 could be divided into three groups: pure rotational emission lines of molecular hydrogen, forbidden emission lines of ions and PAH emission features. In the following sections, we extract physical information from each set of lines, then discuss the possible energy origin of the emission features implied by the properties of the gaseous matter.

4.1 PAH emission features

Detection of PAH emission is uncommon for elliptical galaxies, which could naturally be explained by the rapid destruction due to sputtering by hot plasma. Nevertheless, as mentioned before, NGC 4278 is devoid of an X-ray halo. While strong PAH emission is always related to star-forming activities (Wu et al. 2005), this might not necessarily be the case in elliptical galaxies, since a significant amount of UV photons could be expected for an old stellar population (Binette et al. 1994; Greggio & Renzini 1990). In some limited cases reported, such as Bregman et al. (2006) and Kaneda et al. (2008), PAH emission features in ellipticals show obvious differences from galaxies with active star formation. The band ratio of the 7.7-μm emission feature arising from CC stretching vibrations of PAHs to the 11.3-μm feature arising from CH out-of-plane bending vibrations could be significantly lower than in star-forming regions. This is also the case for NGC 4278, with $I_{7.7}/I_{11.3} = 1.07$. Kaneda et al. (2008) pointed out that while using PAHFIT to derive PAH emission flux, the silicate emission feature around 10 μm originating from outflow winds of AGB stars could lead to significant underestimation of the PAH 7.7 feature. When this feature is subtracted from the original spectrum of NGC 4278, the continuum on the long-wavelength side of PAH 7.7 will be depressed; thus the PAH-7.7 flux derived from fitting will increase significantly, especially when PAH-7.7 emission is weak. To estimate this effect, we subtracted the template of a quiescent elliptical galaxy after scaling it to our spectrum at 5.5 μm (which is an average of three quiescent ellipticals: NGC 1407, NGC 1549 and NGC 3904, kindly provided by Hidehiro Kaneda); the resulting PAH 7.7 emission doubled in flux and gave $I^*_{7.7}/I_{11.3} = 2.03$. In comparison, the median value of $I_{7.7}/I_{11.3}$ is about 4 for H II dominated sources in the *Spitzer* Infrared Nearby Galaxy Survey (SINGS) sample (Smith et al. 2007b), with a minimum of around 2.

In actively star-forming galaxies, a PAH band ratio of 7.7/11.3 has been suggested to reflect the relative proportion of ionized PAHs to neutral PAHs (Galliano et al. 2008), which is further controlled by the intensity of the UV radiation field, electron density and temperature. Meanwhile, the temperature distribution of PAHs could also affect PAH band ratios, while higher average temperatures generally lead to stronger emission at shorter wavelengths. It is still debated, however, as to which factor controls the PAH band ratio in non-star-forming regions such as elliptical galaxies or AGNs. Smith et al. (2007b) compare H II sources with AGNs in the SINGS sample; they found lower ratios of $I_{7.7}/I_{11.3}$ and $I_{11.3}/I_{17}$ for PAH emission in AGNs and also lower ratios of PAH luminosities to total infrared luminosities for AGNs. All these facts are consistent with the scenario that the selective destruction of small PAH molecules and the resulting shift of temperature distribution toward lower temperatures are responsible for PAH band ratios in AGNs. This viewpoint is supported by O'Dowd (2009), who used optical diagnostics to clarify AGNs and star-forming galaxies and found that the difference of PAH band ratios between two regions could be explained by preferential destruction of small PAHs in AGNs. In this sense, NGC 4278 is consistent with the AGN population in all respects. The band ratio $I_{11.3}/I_{17} = 1.75$ also falls in the AGN region of Smith et al. (2007a,b). We further estimate the ratio of total PAH luminosity to total infrared luminosity. Following Dale & Helou (2002) and Smith et al. (2007b), we obtain the total infrared luminosity based on MIPS observations at 24, 70 and 160 μm (data taken from Temi, Brighenti & Mathews 2009). Then we calibrate the total infrared (TIR) luminosity to 8-arcsec aperture based on MIPS 24 luminosity derived from the spectrum. The result gives $L_{\rm totalPAHs}/L_{\rm TIR} = 4.7$ per cent, which is lower than for H II galaxies in the SINGS sample (with a median ∼10 per cent and minimum ∼8 per cent for H II galaxies with metallicity $12 + \log(O/H) > 8.1$).

4.2 Warm molecular hydrogen

Mid-IR molecular hydrogen quadrupole emission lines arising from pure rotational transitions are clearly detected in the central region of NGC 4278. These lines are effective coolants for warm molecular gas with temperature ∼100–1000 K. Excitation mechanisms of H_2 emission include radiative decay after pumping to electronically excited states through the absorption of ultraviolet photons (Morton & Dinerstein 1976), inelastic collision with other particles (Martin, Schwarz & Mandy 1996; Everett & Pogge 1997) and reformation on to excited states for dissociated molecular gas (Hollenbach & McKee 1989). Due to low critical densities (< a few $\times 10^3$ cm^{-3} for S(0)-S(3)), transitions between lower levels are usually thermalized through collisional de-excitation, meaning that pure rotational lines alone are not guaranteed diagnostics to distinguish between different excitation mechanisms.

The radiative decay within pure rotational levels of molecular hydrogen follows quadrupole selection rules; only $\triangle J = -2$ can

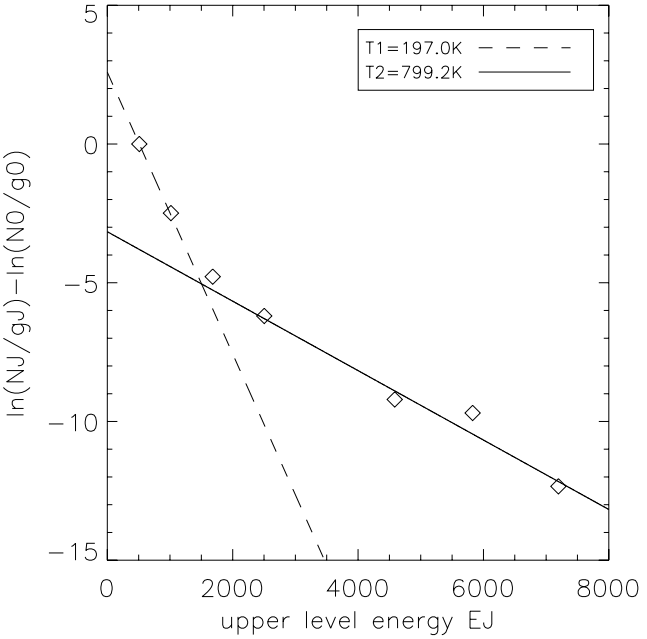

Figure 14. Excitation diagram of H_2 pure rotational lines. The dashed line represents a temperature of 197.0 K, the solid line represents a temperature of 799.2 K. The data point for H_2 S(4) is not shown, since it is blended with PAH 8.6-μm features and could not be accurately decomposed.

occur, where J is the rotational quantum number. The flux of a certain transition could be expressed as $F_{ul} = A_u N_u h\nu_{ul}\Omega/4\pi$, where $u = l + 2$, A_u is the Einstein A coefficient of the upper level, N_u is the column density of molecules on the upper level, $h\nu_{ul}$ is the photon energy and Ω is the beam solid angle. Under the assumption of local thermalization equilibrium (LTE), the fraction of molecules in each state to the total column density could be written as $N_u/N_{total} = g_u \exp[-E_{ul}/kT]/Z(T)$, where g_u is the statistical weight, given by $g_u = (2I + 1)(2l + 1)$; here $I = 0$ for even u and $I = 1$ for odd u. $Z(T)$ is the partition function. We adopt $Z(T) = 0.0247T/[1 - \exp[6000K/T]$ (Herbst et al. 1996), which is valid for $T > 40$ K.

Fig. 14 shows the excitation diagram for the central 8-arcsec region of NGC 4278. Emission lines up to S(7) are detected above the 3σ level, except for S(4), which could be obscured by the PAH 7.7 feature. The fit of S(6) is highly affected by the adjacent 6.2-μm PAH feature. We estimate the uncertainty of S(6) by fitting 100 randomly noise-added spectra within the noise limit; the result estimated in this way is in consistent with that directly derived from PAHFIT, with a mean flux of 1.8×10^{-21} erg s^{-1}. Data points in our diagram do not show obvious sign of an ortho-to-para ratio (OPR) deviating from thermal equilibrium below the $J = 8$ level, which would appear as a 'zigzag' pattern between ortho states and para states (Neufeld et al. 2006). We thus use a two-temperature model with $OPR = 3$ (equilibrium value) to fit all data points. The result gives a warm component $T_w \sim 197$ K with column density $N_{Hw} = 0.75 \times 10^{20}$ cm^{-3} and a hot component ($T_h \sim 799$ K) with $N_{Hh}{}^{hot} = 1 \times 10^{18}$ cm^{-3}, corresponding to a mass of 1.49×10^6 M$_\odot$ within an 8-arcsec aperture. This result remains almost unchanged if we apply lines derived from the 'matched spectrum', which lowers S(1) by 10 per cent and S(0) by 18 per cent; the two temperatures given in this case are $T_w \sim 206$ K and $T_h \sim 811$ K.

Roussel et al. (2007) carried out a systematic research on H_2 pure rotational emission based on the SINGS galaxies sample. They suggest that H_2 rotational lines in nearby star-forming galaxies are dominated by emission from photon dissociation regions (PDR), while in AGN objects excess H_2 emission could be excited through shock heating. In NGC 4278, molecular hydrogen shows a higher excitation temperature than most galaxies in the SINGS sample, in which only three galaxies classified as AGN objects are detected with lines higher than S(3). To compare NGC 4278 with SINGS galaxies, we follow Roussel et al. (2007) and use only S(0)–S(3) to fit a two-temperature model, which gives a warm component $T_w \sim 189$ K with $N_{Hw} = 2.1 \times 10^{20}$ cm^{-3} and a hot component $T_h \sim 701$ K with $N_{Hh} = 4 \times 10^{18}$ cm^{-3}. The temperature of the warm component and the fraction of the hot component are still higher compared with most SINGS galaxies. Meanwhile, this temperature is lower than for stellar-scale shock-heated regions, such as supernova remnants (Neufeld et al. 2007; Hewitt et al. 2009) and Herbig–Haro objects (Neufeld et al. 2006), but similar to that for some recently discovered galaxy-scale shocks (Appleton et al. 2006; Ogle et al. 2007). Furthermore, CO emission has been detected in NGC 4278 with IRAM observations (Combes et al. 2007). This allows us to calculate the fraction of warm H_2 to cold H_2. We assume that the excitation temperature of warm H_2 stays constant and calibrate the mass from 8-arcsec aperture to 23-arcsec aperture based on the flux of H_2 S(1), where 23 arcsec is the beam size of IRAM, to derive the cold H_2 mass. The result gives M(warm H_2)/M(cold H_2) = 0.10, somehow larger than the typical value in the SINGS sample.

A three-temperature model would not achieve a significantly better result, because energy levels higher than $J = 7$ do not lie along a straight line and could not be fitted by a simple temperature component. One possible explanation is that the S(6) line ($J = 8$) is overestimated, since this line is blended with [Ar II] emission and might not be well decomposed. Otherwise, if S(6) and S(7) are measured accurately, higher rotational levels with $J > 7$ might indicate an OPR lower than 3. Unfortunately, without a reliable measurement of S(4), which is blended with the PAH 8.6 feature, we are not able to discern between different possibilities.

4.3 Fine-structure line emission

The nuclear spectra of NGC 4278 show abundant emission lines arising from low-level forbidden transitions of different ionic species, including [Ar II] 7.0 μm, [S IV] 10.5 μm, [Ne II] 12.8 μm, [Ne III] 15.6 μm, [O IV] & [Fe II] 26-μm blend, [S III] 18.7 μm, [S III] 33.5 μm as well as [Si II] 34.8 μm. These lines provide valuable information about the physical state of warm gas. The ratio of [Ne III]/[Ne II] is commonly used as an indicator of ionization states, and has a value of 0.81 for the nuclear region of NGC 4278. This is a typical value found in LINER objects and cannot help us distinguish between star-forming regions, AGNs and shock-heated regions (Allen et al. 2008; Dale et al. 2009).

The most distinctive feature of the fine-structure emission in NGC 4278 is the strong [Si II] 34.8-μm emission located at the red end of the spectrum, which could be compared with the nearby [S III] 33.5-μm line and shows a ratio of [Si II] 34.8 μm/[S III] 33.5 μm = 5.9. This ratio is higher than any for SINGS galaxies (Dale et al. 2009) and resembles values observed in shock-dominated regions, such as supernova remnants (Neufeld et al. 2007) and large-scale shocks triggered by galaxy interactions (Cluver et al. 2010), in which [Si II] emission is boosted by the sputtering destruction of dust during a fast shock, since as an element of high depletion a large fraction of Si is locked in dust in the diffuse ISM. Dale et al. (2009) find a separation of the [Si II]/[S III] ratio between AGNs and H II galaxies in the SINGS sample, while AGNs show stronger [Si II] emission. In their

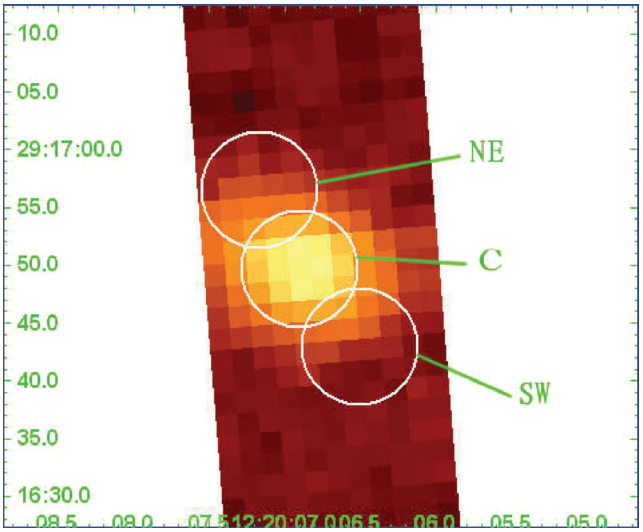

Figure 15. PAH 11.3 map, overplotted with three neighbouring extraction apertures, each with a 5-arcsec radius: north-east (NE, centred at 185.02986,29.28235), central (C, centred at 185.02875,29.28048) and south-west (SW, centred at 185.02802, 29.27872).

discussion, this separation might be caused by reduced depletion of silicon, X-ray photoionization processes or an increased density for emission gas. The last possibility, however, seems unlikely to be applicable to NGC 4278. The electricity density derived from the ratio of [S III] 18.7 μm/[S III] 33.5 μm, with a value of 0.69, is close to the low-density limit and indicates that the bulk of the fine-structure emission comes from regions with density around 300 cm^{-3} (Giveon et al. 2002). On the other hand, it is also doubtful that X-ray photoionization plays a major role in boosting [Si II] emission in the nuclear region of NGC 4278, which holds a low luminosity active galactic nuclei (LLAGN) with moderate hard X-ray luminosity $L_{2-10\,keV} = 10^{40.4}$ erg s^{-1}, since, as mentioned above, the ionization of extended gas is not dominated by AGN photoionization and the [Si II] line distribution shows a widely extended structure. We will see in Section 4.5 that a high [Si II]/[S III] ratio still appears in the area more than 1 kpc away from the nucleus.

4.4 Radial emission-line distributions

It is important to understand the excitation mechanism of the extended emission in the central region. However, the results given above are based on the spectra extracted from the central 8-arcsec aperture and cannot avoid being mixed with an AGN component. It is thus very useful to quantitatively explore the spatial distributions of different emission features further. Unfortunately, both the limited mapping area of the SL module and the imperfect calibration for extended emission pose obstacles. In this section, we extract spectra from three adjacent apertures of 5-arcsec radius, with one centred at the continuum peak of the spectral map and two centred north-east (NE) and south-west (SW) of the galaxy centre, as shown in Fig. 15. The 5-arcsec aperture size is somewhat small for the extraction of LL orders due to its large pixel size and extended PSF, hence comparisons of the radial distribution of different lines based on LL observations should be taken with caution. Therefore, here we only focus on SL spectra. The spectra are presented in Fig. 16 and the detected line fluxes are shown in Table 2.

While [Ne III] 15.6 μm/[Ne II] 12.8 μm is a comfortable indicator of ionization states, [Ne III] falls in the LL wavelength range. Here

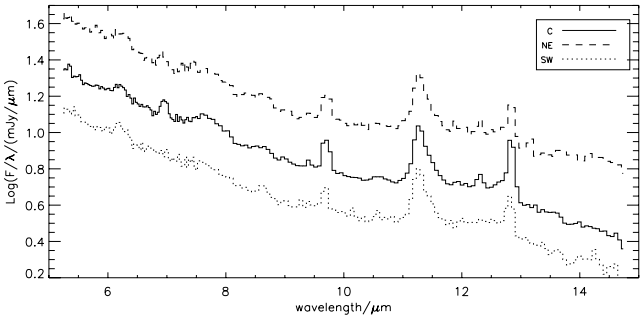

Figure 16. Scaled SL spectra extracted from the three apertures shown in Fig. 14. The solid line represents the result from the central aperture, the dashed line represents the result from the north-east aperture and the dotted line represents the result from the south-west aperture.

Table 2. Emission-line strengths in three neighbouring 5-arcsec apertures.

Line	NE (10^{-21} W cm^{-2})	C (10^{-21} W cm^{-2})	SW (10^{-21} W cm^{-2})
PAH 6.2 μm	3.63 ± 0.12	8.63 ± 0.14	2.79 ± 0.15
PAH 7.7 μm	16.05 ± 1.06	51.77 ± 1.10	12.86 ± 1.03
PAH 11.3 μm	8.67 ± 0.17	22.10 ± 0.15	5.96 ± 0.13
PAH 12.6 μm	2.83 ± 0.29	9.03 ± 0.30	3.04 ± 0.12
H_2 S(2)	0.33 ± 0.04	0.98 ± 0.05	0.15 ± 0.04
H_2 S(3)	1.21 ± 0.05	4.08 ± 0.06	0.79 ± 0.06
H_2 S(5)	0.74 ± 0.15	2.46 ± 0.18	<0.34
H_2 S(6)	0.44 ± 0.14	1.15 ± 0.14	0.49 ± 0.14
H_2 S(7)	<0.43	0.75 ± 0.15	<0.46
[Ar II] 7.0 μm	<0.54	2.34 ± 0.17	<0.36
[S IV] 10.5 μm	0.16 ± 0.05	0.33 ± 0.06	0.16 ± 0.05
[Ne II] 12.8 μm	1.00 ± 0.04	4.46 ± 0.06	0.67 ± 0.03
9.0 μm[a]	7.85 ± 0.21	20.40 ± 0.23	6.01 ± 0.18

[a] 9.0 continuum flux densities are given in units of mJy.

we use [S IV] 10.5 μm/[Ne II] 12.8 μm as a substitute diagnostic of gas ionization. The validity of this approach has been verified by Groves, Nefs & Brandl (2008). We find that the [S IV]/[Ne II] in the two extended regions, NE and SW, are higher than in the central region, although in both cases the [S IV] fluxes are barely higher than the 3σ level. The [S IV]/[Ne II] ratio is 0.16 in the NE region and 0.24 in the SW region, in comparison with 0.08 in the central region. This result is consistent with the distribution of [O III]λ5007/Hβ derived from SAURON observations and confirms that a significant fraction of extended emission is not excited by central AGN photoionization even within the central 10-arcsec region.

It is also interesting to explore any possible variation of the PAH band ratio in the three regions. However, we found that PAH 6.2/PAH 7.7 ratios directly derived from PAHFIT in the three regions are larger than 0.5 and cannot be explained by any PAH model (Draine & Li 2001). We suggest that such an unphysical value of PAH 6.2/7.7 appeared because we failed to consider the silicate emission as we did in Section 4.1, thus underestimating the PAH-7.7 flux. When a template of silicate emission is subtracted from the original spectra, the fitting results are as given in Table 2. Our results show that both PAH 6.2/7.7 and PAH 7.7/11.3 have no significant spatial variation, while PAH 6.2/7.7 is slightly lower in the centre and PAH 7.7/11.3 is higher in the centre. This may suggest more large, neutral PAHs in the galaxy centre relative to the outer area, which could be a result of either a hard radiation process from the AGN or a shock process while gas flows into the centre.

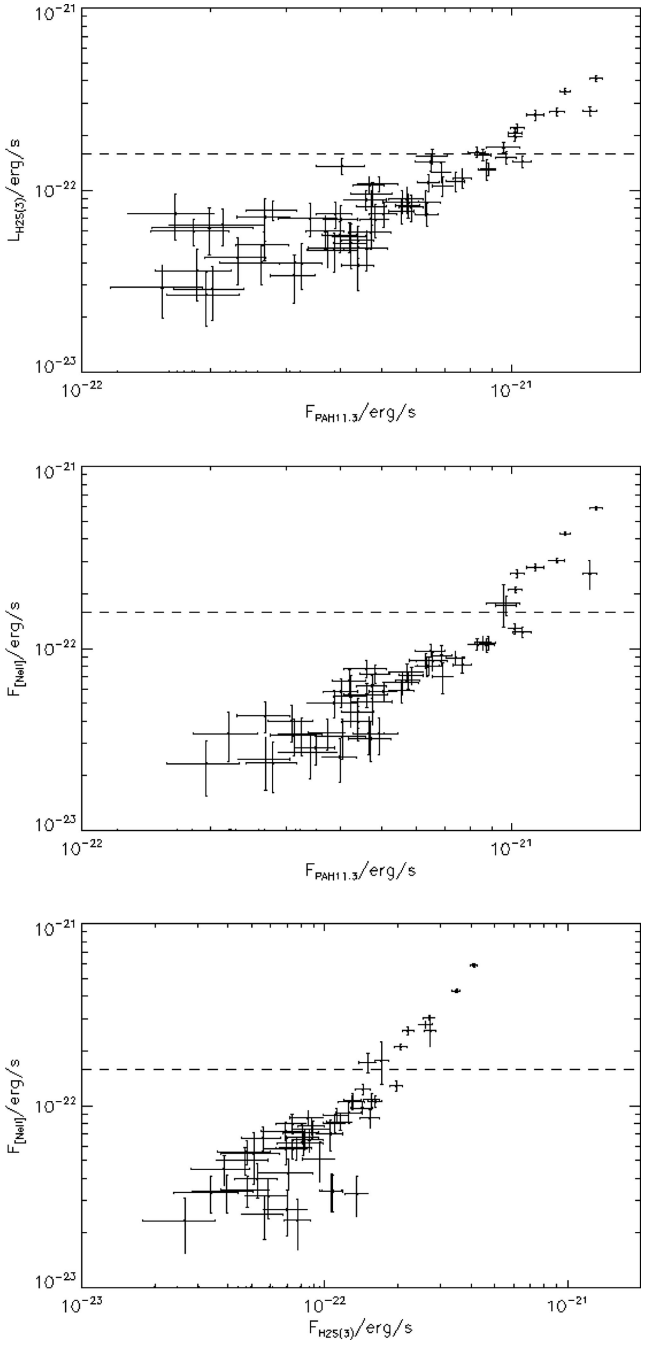

Figure 17. Pixel-to-pixel plots for the central 9 × 11 pixels of the SL mode spectral map. Upper panel: H_2 S(3) to PAH 11.3. Middle panel: [Ne II] to PAH 11.3. Lower panel: [Ne II] to H_2 S(3). The dashed line marks pixels where the slope starts to change.

In Fig. 17, we show pixel-to-pixel comparisons between [Ne II] 12.8 μm, PAH11.3 μm and H_2 S(3) for the central 11 × 9 pixels of the SL map. It is obvious that [Ne II] 12.8 μm shows distinct slope changes for the most luminous 9 pixels, which corresponds to a central region of about <3 arcsec. This should be a sign that the AGN continuum starts to dominate the heating in this region and produces relatively more high-ionization nebula-line emission relative to PAH emission and warm molecular emission. This result confirms the SAURON result that [O III]λ5007/Hβ starts to decline on entering the central 5-arcsec area. Another sign revealed by

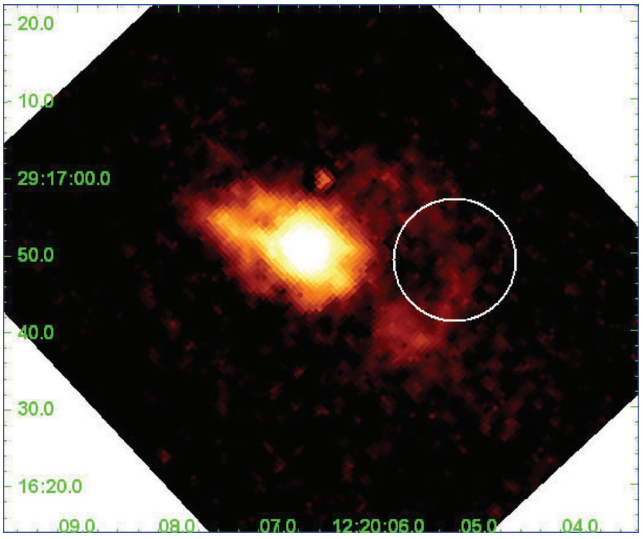

Figure 18. Image of IRAC 8.0 non-stellar emission, overplotted with the extraction aperture for the high-ionization region, which is centred at (185.02190,29.28036), with a radius of 8 arcsec.

Fig. 17 is enhanced H_2 S(3) emission toward the outermost area, relative to both [Ne II] and PAH 11.3, which appears as a shallower slope in the H_2 S(3) to PAH 11.3-μm plot and excessive H_2 S(3) in the [Ne II] 12.8-μm to H_2 S(3) plot. Enhanced H_2 S(3) toward the outer area is consistent with our finding that H_2 S(1) is more extended than both PAH emission and nebula lines.

4.5 Spectra in the western high-ionization region

We further explore the ionization and excitation states for gas in the western high-ionization, low-surface-brightness region as revealed by SAURON observations. We extract LL spectra from an 8-arcsec aperture centred at the west of the nucleus, as shown in Fig. 18. The flux of emission lines are given in Table 3. Unlike the nuclear region, here we employ SLCF to correct spectra since there should be considerable outgoing light from the nearby bright nuclear region diffracted into the local area. The spectrum is given in Fig. 19, compared with the spectrum extracted from the central area. For the high-ionization region, the continuum emission longer than 20 μm shows a shallower slope than the spectra of the central region; this difference remains when we compare it with the SLCF-corrected central spectrum, which, as discussed above, flattens the continuum at wavelengths longer than 20 μm. We can quantify the slope at wavelengths longer than the 20-μm continuum simply by the ratio of the final fitted continuum at 36 μm to that at 21 μm. For the

Table 3. Emission-line strengths in the high-ionization region.

Line	Flux (10^{-21} W cm $^{-2}$)
PAH 17 μm	2.24 ± 0.38
H_2 S(0)	<0.12
H_2 S(1)	0.85 ± 0.07
[Ne III] 15.6 μm	0.30 ± 0.06
[S III] 18.7 μm	<0.19
[S III] 33.5 μm	0.26 ± 0.06
[Si II] 34.8 μm	0.95 ± 0.10

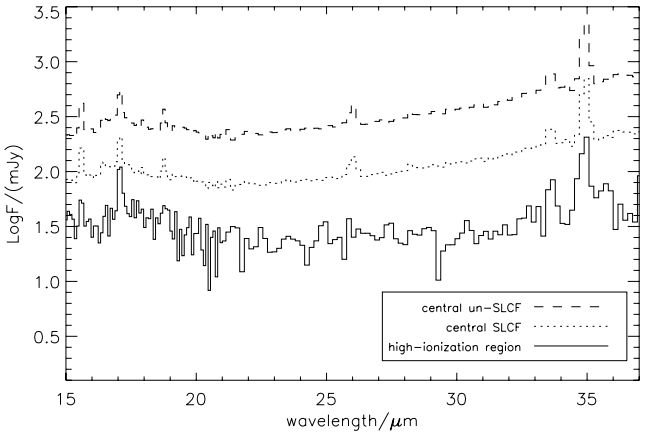

Figure 19. Scaled LL spectra (solid) extracted from the aperture shown in Fig. 17. For comparison, the central 8-arcsec matched spectra (dotted line) and uncorrected spectra (dashed line) are scaled and plotted.

central region with slit-loss correction $F36/F21 = 2.7$, for the central region without SLCF $F36/F21 = 3.1$, while in the high-ionization region the ratio is 1.9. The lack of a hot dust component, as indicated by the shallower continuum, could be a natural result of a weaker UV–optical continuum or larger sizes of local dust grain.

The high-ionization region is characterized by an enhanced H_2 S(1) emission. The relative strength of H_2 S(1) to nearby [Ne III] 15.6 μm, [S III] 18.7 μm ionized emission and the underlying PAH 17-μm feature in the high-ionization region is increased by a factor of 2 or more. Meanwhile, the excitation temperature derived from H_2 S(1) and H_2 S(0) is >183 K. Without information from higher level lines, this result indicates a temperature not lower than the central region if assuming an equilibrium OPR. The enhancement of H_2 S(1) is consistent with that shown in Fig. 6; the distribution of H_2 S(1) narrow-band emission exhibits an extended component to the west of the nuclei. In the next section we will discuss the possible origin of this feature.

5 DISCUSSION: THE ORIGIN OF EXTENDED WARM GAS AND DUST

Results from *Spitzer* mapping observations reveal abundant warm dust, molecular gas and ionized gas in the central region of NGC 4278. One or more additional ionization sources apart from AGN photoionization is required to explain the extended ionized gas. It is conceivable that the energy source responsible for extended warm gas is also related to the physical properties of extended dust and molecular hydrogen we observed. In this section, we will discuss possible heating mechanisms that could offer a self-consistent explanation for the different phases of extended dusty gas.

The detection of both PAHs and cold molecular gas might imply some degree of residual star formation, while it seems unlikely that star-forming activity plays an important role in the case of NGC 4278. Infrared emission lines of NGC 4278 show a behaviour distinct from that expected for a PDR (Kaufman, Wolfire & Hollenbach 2006). Also, barely any sign of star-forming activity is shown at any wavelength in the central kpc region. Galaxy Evolution Explorer (GALEX) observations show that NGC 4278 should be classified as a typical UV upturn galaxy based on the strong far-ultraviolet (FUV) emission throughout the galaxy; this is direct evidence that the background radiation field is possibly from a hotter old stellar population (post-AGB, LMXB or EHB) instead of OB stars. Additionally, in Sarzi et al. (2010) the authors have quantitatively explored the ionization mechanism for NGC 4278 based on a comparison between the emission-line diagnostics and predictions of MAPPING-III models (section 3.4.1, fig. 12). Their results show that ionized gas in NGC 4278 clearly falls outside the star-formation region in the emission-line diagram. The extended ionized gas in NGC 4278 exhibits LINER-type emission lines, which further casts doubt on the idea that ionized gas is not heated by young stars.

Regarding stellar population analysis, previous research shows different results for the stellar population of NGC 4278, while Serra et al. (2008) reported a 3-Gyr single stellar population in the circumnuclear region of NGC 4278, Zhang, Gu & Ho (2008) and recent SAURON results (Kuntschner et al. 2010) only gave a 10-Gyr stellar population.

If the bulk of extended atomic, molecular and dust emission comes from a star-forming area, a similar spatial distribution should be expected for different types of emission lines; such a coincidence is also not observed, suggesting that at least a second physical process is acting.

Another commonly employed heating mechanism in elliptical galaxies is the processes related to X-ray-emitting hot gas, such as cooling flows from hot gas and evaporation flows caused by interaction between cold and hot gas (Sparks et al. 1989; de Jong et al. 1990). Still, this possibility is easily ruled out. NGC 4278 shows no X-ray halo and, as can be seen in Fig. 10, the diffuse soft X-ray emission in the central region seems to trace cold and warm gas and is too weak to serve as an efficient energy reservoir in order to explain the observed strong optical and infrared emission.

Based on SAURON results, Sarzi et al. (2010) suggest that warm gas in early-type galaxies is generally powered by evolved stellar sources, especially post-AGB stars, based on their calculation that an old stellar population is able to provide sufficient ionizing photons for the observed warm gas as well as the fact that the surface brightness of Hβ emission is tightly correlated with that of local optical continuum emission. The latter phenomenon was previously pointed out by Macchetto et al. (1996). In Sarzi et al. (2010), the results reveal the unusual ionization structure of NGC 4278. However, the dominant ionization source in NGC 4278 could still be photoionization by UV radiation from old stars instead of fast shocks, based on the fact that high-ionization regions are characterized by low surface brightness of Hβ emission, which contrasts with the common case for shock-heated regions. They also argued that the shock velocity predicted by shock models (300–500 km s^{-1}, depending on whether a H II precursor is introduced) is too large to maintain a stable rotational pattern as seen in NGC 4278.

Nevertheless, a dynamical environment giving birth to hundred-to-thousand pc scale shocks is not unexpected for the centre of NGC 4278. As shown by Sarzi et al. (2006), the kinematics of ionized gas is different from that of stars, with the position angle of the rotation axis showing a maximum deviation from that of the stars at the outermost region, while this misalignment angle between stars and gas gradually decreases toward the inner region and reaches a minimum at the galaxy centre. This kinematic feature is not difficult to understand. Morganti et al. (2006) point out that the central rotational structure of warm gas in NGC 4278 seems to be just a subcomponent of the large extended H I disc. It is commonly recognized that massive cold gas disc in elliptical galaxies is usually a product of merging with a gas-rich galaxy. The faint tail-like features in the H I map of NGC 4278 also support this idea. Therefore, shocks triggered by random collisions between gas clouds could possibly happen when gas is accreted from the extended H I disc to

the central stellar gravitational well. It is worthwhile noting that the western high-ionization region shown in Fig. 3 exactly corresponds to the area in the velocity map at which gas experiences a turning of position angle (Sarzi et al. 2006).

Our observational results reveal several possible signs of a shock process happening in the central region of NGC 4278. As discussed above, the extended strong emission of [Si II] could be explained by sputtering destruction of silicate dust grains in the fast shock process instead of X-ray photoionization by the central AGN; this is further supported by the possibly modified size distribution of PAHs, as implied by different PAH band ratios. Recently, Kaneda et al. (2010) showed that in NGC 4589, another PAH-detected elliptical sharing similar infrared spectral features with NGC 4278, the PAH 17 distribution is different from that of PAH 11.3 emission. The authors explain this segregation by saying that PAH 11.3 arises from newly formed PAHs when dusty gas falls toward the centre. In Fig. 5 we find similar results, which may imply that PAHs are undergoing reprocessing in an extended area. On the other hand, spatially the X-ray diffuse emission follows the main features of ionized gas, molecular species and dust. The temperature of the thermal component found by Younes et al. (2010), 0.4 ± 0.1 keV within a 10-arcsec aperture, indicates a shock velocity of $\sim$600 km s^{-1} (Draine & McKee 1993) and is higher than expected from optical-line diagnostics. However, the authors also point out that the central diffuse emission may contain more than one temperature component, with less-hot components in the extended region.

We find an excess luminosity of molecular hydrogen rotational lines populating high excitation temperatures compared with PDR regions of star-forming galaxies, with respect to the aromatic bands, 24-μm continuum, total IR luminosity and [Si II] 34.8-μm emission (Roussel et al. 2007). This component of extended warm molecular hydrogen associated with highly ionized gas also provides evidence for an extended shock. Enhanced emission from warm molecular hydrogen is found for AGN objects in the SINGS sample and stellar-/galactic-scale shock-heated regions. Roussel et al. argue that X-ray excitation seems unlikely to be responsible for excess warm molecular hydrogen in the SINGS AGN subsample; instead they suggest a fast shock triggered by dynamical perturbations as the heating source. Furthermore, we have found an extended high-ionization region related to enhanced H_2 S(1) emission. These facts support the idea that X-ray excitation from the central AGN cannot explain the observed excess, high-excitation-temperature H_2 emission. A second heating mechanism could be also supported by the possible deviation of the H_2 S(1) peak from other lines as shown in Fig. 6. On the other hand, there is no evidence of dynamical perturbation directly related to the central AGN. Although it is classified as a FR I radio galaxy, the radio jet of NGC 4278 is confined to milliarcsec scales and shows a direction approximately perpendicular to the elongated main feature of warm gas (Falcke et al. 2000). The *Hubble Space Telescope* (*HST*) STIS high-spatial-resolution observations also indicate that the twist of velocity field only happens within the inner 0.5-arcsec region (Walsh et al. 2008).

Guillard et al. (2009) develop a common scenario to interpret the dominance of warm H_2 emission in dynamically disturbed regions, in which pre-shock gas exists in both high-density clouds and low-density intercloud gas. Under a higher shock velocity, the low-density, diffuse gas is heated to plasma with temperature a few $\times 10^6$ K, while the dusty clouds heated to lower than 10^6 K cool efficiently, dissipating their kinematic turbulent energy into H_2 emission through a slow shock. This scenario is consistent with our finding that the distribution of H_2 emission and PAH emission are similar, while both depart from ionized emission. It provides a natural explanation for the anticorrelation between the 8-μm PAH feature and [O III]λ5007/Hβ shown in Fig. 3, since PAHs are expected to be entirely destroyed in fast-shock-heated plasma (Micelotta, Jones & Tielens 2010). If so, the decreased [Si II]/[S III] ratio in this region might be a result of relatively more pre-shock gas distributed in high-density clouds.

It is uncertain, however, whether the shock component revealed by the above evidence could be responsible for the bulk of gas ionization in the central elongated feature. The optical and infrared fine-structure line diagnostics allowed by current data are not sufficient to distinguish clearly between UV photoionization and fast shocks. Although there are abundant optical spectral observations for NGC 4278 (Rose & Tripicco 1984; Ho et al. 1997; Walsh et al. 2008), these observations are usually based on a slit centred at the central AGN. We notice that due to a detectable high-excitation line [O III]λ4363 in its optical slit spectrum, NGC 4278 was suggested as a possible example of a shock-excited LINER (Rose et al. 1984). An obstacle in viewing shock heating as the main ionization mechanism is the low surface brightness of the high-ionization area. Interestingly, we find a discrepancy between fine-structure lines with different ionization potentials, with the highest ionization mapped line, [Ne III] 15.6 μm, showing the most symmetrical distribution. A much lower [Ne III]/[Ne II] is expected to be produced in the shock region than in gas ionized by FUV radiation (Spinoglio & Malkan 1992; Allen et al. 2008). If this feature is further confirmed, it implies that shock heating may play a role in the excitation of lower ionized species in an extended region.

6 CONCLUSION

We performed *Spitzer* IRS spectral mapping observations toward the central region of the nearby elliptical galaxy NGC 4278. We discovered rich emission features produced by warm dust, molecular hydrogen and ionized gas in the galaxy centre. The multiphases of warm and hot gas generally coincide well with the optical line distribution, suggesting they belong to the same structure. We confirm the reverse distribution of ionization states shown in optical observations. The spectrum of the nuclear region is characterized by strong [Si II] 34.8-μm emission, which is naturally explained by reduced silicon depletion through dust sputtering. The PAH band ratios in the nuclear region could be interpreted by modified size due to selective destruction against small grains; in particular, the PAH 7.7 μm/11.3 μm ratio decreases while moving away from the nucleus, indicating a high fraction of neutral PAHs or a deficiency of small PAHs in the outer region. The warm molecular hydrogen shows excessive emission arising from pure rotational transitions with respect to both dust and ionized emission lines; the excitation diagram of pure rotational lines gives a high excitation temperature similar to some galactic shock-heated regions. We found a high-ionization extended region associated with enhanced rotational molecular emission. We conclude that a shock region on the hundred-to-thousand pc scale triggered by interaction between clouds and diffuse cold gas accreted from the outer region of the galaxy should exist within the dynamically perturbed environment in the centre of NGC 4278, while the contribution of this shock component to the total ionization of gas is still unclear.

ACKNOWLEDGMENTS

The authors are very grateful to Marc Sarzi and Hidehiro Kaneda for providing SAURON data of NGC 4278 and IRS spectra of quiescent elliptical galaxies. This research made use of Tiny Tim/Spiter,

developed by John Krist for the *Spitzer* Science Center. The Center is managed by the California Institute of Technology under a contract with NASA. The authors also acknowledge financial support from the Natural Science Foundation of China under grants 10878010 and 10633040, and the National Basic Research Program (973 program No. 2007CB815405). This research has made use of NASA's Astrophysics Data System Bibliographic Services and the NASA/IPAC Extragalactic Data base (NED), which is operated by the Jet Propulsion Laboratory, California Institute of Technology, under contract with the National Aeronautics and Space Administration. This work is based on observations made with the *Spitzer* Space Telescope, which is operated by the Jet Propulsion Laboratory, California Institute of Technology, under NASA contract 1407.

REFERENCES

Allen M. G., Groves B. A., Dopita M. A., Sutherland R. S., Kewley L. J., 2008, ApJS, 178, 20
Appleton P. N. et al., 2006, ApJ, 639, 51
Binette L., Magris C. G., Stasinska G., Bruzual A. G., 1994, A&A, 292, 13
Bregman J. N., Temi P., Bregman J. D., 2006, ApJ, 647, 265
Cluver M. E. et al., 2010, ApJ, 710, 248
Combes F., Young L. M., Bureau M., 2007, MNRAS, 377, 1795
Dale D. A., Helou G., 2002, ApJ, 576, 159
Dale D. A. et al., 2009, ApJ, 693, 1821
de Jong T., Norgaard-Nielsen H. U., Jorgensen H. E., Hansen L., 1990, A&A, 232, 317
Dopita M. A., Sutherland R. S., 1995, ApJ, 455, 468
Draine B. T., Li A., 2001, ApJ, 551, 807
Draine B. T., McKee C. F., 1993, ARA&A, 31, 373
Everett M. E., Pogge R. W., 1997, in Malbet F., Castets A., eds, Proc. IAU Symp. 182, Low Mass Star Formation – From Inflow to Outflow. Poster Proceeding, p. 106
Fabian A. C., 1994, ARA&A, 32, 277
Falcke H., Nagar N. M., Wilson A. S., Ulvestad J. S., 2000, ApJ, 542, 197
Fazio G. G. et al., 2004, ApJS, 154, 10
Filippenko A., 2003, in Collin S., Combes F., Shlosman I., eds, ASP Conf. Ser. Vol. 290, Active Galactic Nuclei: From Central Engine to Host Galaxy. Astron. Soc. Pac., San Francisco, p. 369
Galliano F., Madden S. C., Tielens A. G. G. M., Peeters E., Jones A. P., 2008, ApJ, 679, 310
Giveon U., Sternberg A., Lutz D., Feuchtgruber H., Pauldrach A. W. A., 2002, ApJ, 566, 880
Goudfrooij P., de Jong T., Hansen L., Norgaard-Nielsen H. U., 1994, MNRAS, 271, 833
Greggio L., Renzini A., 1990, ApJ, 364, 35
Groves B., Nefs B., Brandl B., 2008, MNRAS, 391, 113
Guillard P., Boulanger F., Pineau D. F. G., Appleton P. N., 2009, A&A, 502, 515
Herbst T. M., Graham J. R., Tsutsui K., Beckwith S., Matthews K., Soifer B. T., 1996, AJ, 99, 1773
Hewitt J. W., Rho J., Andersen M., Reach W. T., 2009, ApJ, 694, 1266
Ho L. C., Filippenko A. V., Sargent W. L. W., 1997, ApJS, 112, 315
Hollenbach D., McKee C. F., 1989, ApJ, 342, 306
Jeong H. et al., 2009, MNRAS, 398, 2028
Kaneda H., Onaka T., Sakon I., Kitayama T., Matsumoto H., Suzuki S., 2008, ApJ, 684, 270
Kaneda H., Onaka T., Sakon I., Kitayama T., Okada Y., Suzuki T., Yishihara D., Yamagishi M., 2010, ApJ, 716, 161
Kaufman M., Wolfire M., Hollenbach D. J., 2006, ApJ, 644, 283
Knapp G. R., Turner E. L., Cunniffe P. E., 1985, AJ, 90, 454
Knapp G., Guhathakurta R., Kim D.-W., Jura M. A., 1989, ApJS, 70, 329
Kuntschner H. et al., 2010, MNRAS, 408, 97
Lauer T. R. et al., 2005, AJ, 129, 2138
Macchetto F., Pastoriza M., Caon N., Sparks W. B., Giavalisco M., Bender R., Capaccioli M., 1996, A&AS, 120, 463
Martin P. G., Schwarz D. H., Mandy M. E., 1996, ApJ, 461, 265
Micelotta E. R., Jones A. P., Tielens A. G. G. M., 2010, A&A, 510, 36
Morganti R. et al., 2006, MNRAS, 371, 157
Morton D. C., Dinerstein H. L., 1976, ApJ, 204, 1
Neufeld D. A. et al., 2006, ApJ, 649, 816
Neufeld D. A., Hollenbach D. J., Kaufman M. J., Snell R. L., Melnick G. J., Bergin E. A., Sonnentrucker P., 2007, ApJ, 664, 890
Noordermeer E., 2006, PhD thesis, Rijksuniversiteit Groningen
O'Dowd M. J., 2009, ApJ, 705, 885
Ogle P., Antonucci R., Appleton P. N., Whysong D., 2007, ApJ, 668, 6990
Oosterloo T. A., Morganti R., Sadler E. M., Vergani D., Caldwell N., 2002, AJ, 123, 729
Rose J. A., Tripicco M. J., 1984, ApJ, 285, 55
Roussel H. et al., 2007, ApJ, 669, 959
Sage L. J., Welch G. A., Young L. M., 2007, ApJ, 657, 232
Sarzi M. et al., 2006, MNRAS, 366, 1151
Sarzi M. et al., 2010, MNRAS, 402, 2187
Serra P., Trager S. C., Oosterloo T. A., Morganti R., 2008, A&A, 483, 57
Smith J. D. T. et al., 2007a, PASP, 119, 1133
Smith J. D. et al., 2007b, ApJ, 656, 770
Sparks W. B., Macchetto F., Golombek D., 1989, ApJ, 345, 153
Spinoglio L., Malkan M. A., 1992, ApJ, 399, 504
Tang Y.-P., Gu Q.-S., Huang J.-S., Wang Y.-P., 2009, MNRAS, 397, 1966
Temi P., Brighenti F., Mathews W. G., Bregman J. D., 2004, ApJS, 151, 237
Temi P., Brighenti F., Mathews W. G., 2009, ApJ, 695, 1
Terashima Y., Wilson A. S., 2003, ApJ, 583, 145
Tonry J. L., Dressler A., Blakeslee J. P., Ajhar E. A., Fletcher A. B., Luppino G. A., Metzger M. R., Moore C. B., 2001, ApJ, 546, 681
Walsh J. L., Barth A. J., Ho L. C., Filippenko A. V., Rix H.-W., Shields J. C., Sarzi M., Sargent W. L. W., 2008, AJ, 136, 167
Wiklind T., Combes F., Henkel C., 1995, A&A, 297, 643
Wu H., Cao C., Hao C.-N., Liu F.-S., Wang J.-L., Xia X.-Y., Deng Z.-G., Young C. K.-S., 2005, ApJ, 632, 79
Younes G., Porquet D., Sabra B., Grosso N., Reeves J. N., Allen M. G., 2010, A&A, 517, 33
Zhang Y., Gu Q. S., Ho L. C., 2008, A&A, 487, 177

This paper has been typeset from a TEX/LATEX file prepared by the author.